Chemical Manipulation of the Spin-Crossover Dynamics through Judicious Metal-Ion Dilution

Xiang Li, Dong Zhang, Yuqing Qian, Wenxuan Liu, Corine Mathonière, Rodolphe Clérac, Xin Bao

Chemical Manipulation of the Spin-Crossover Dynamics through Judicious Metal-Ion Dilution

Xiang Li, Dong Zhang, Yuqing Qian, Wenxuan Liu, Corine Mathonière,* Rodolphe Clérac,* and Xin Bao*

In 2019, our groups described a unique Fe^{II} complex, $[Fe(^{2Me}L)(NCBH_3)_2]$ (^{2Me}L = *N,N′*-dimethyl-*N,N′*-bis-(2-pyridylmethyl)-1,2-ethanediamine) possessing a low-spin ground state that is not easily accessible due to the extremely slow dynamics of the high-spin to low-spin phase transition. Herein, we report the successful chemical manipulation of this spin-crossover (SCO) process through controlled metal-ion dilutions. The emergence or suppression of the thermally induced SCO behavior was observed depending on the radius of the metal ion used for the dilution (Ni^{II} or Zn^{II}). Reversible photo-switching has been confirmed in all mixed-metal complexes whether the low-spin state is thermally accessible. Remarkably, the dilution with Zn^{II} metal ions stabilizes HS Fe^{II} complexes with complete suppression of the thermally induced SCO process without destroying the reversible photoswitchability of the material.

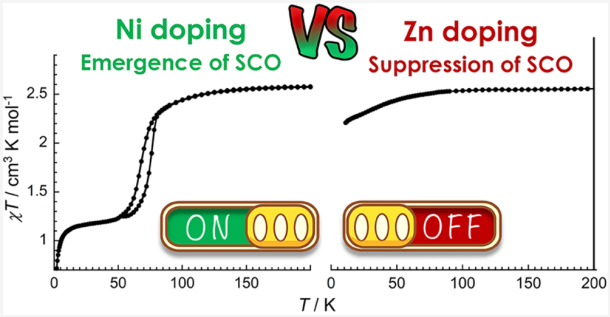

INTRODUCTION

The spin-crossover (SCO) phenomenon is considered as one of the most attractive switching processes in material sciences. Commonly, SCO compounds possess two magnetic states, a low-spin (LS) state and a high-spin (HS) state, which can be addressed upon temperature, light, pressure, chemical, or magnetic-field stimuli.[1−5] These switchable materials have been of interest to diverse fields of applications, such as ultrahigh-density data storage devices, molecular switches, molecular actuators, logic gates, optical/electronic devices, and sensors.[6−11] The origin of the SCO phenomenon is molecular and is associated with a significant change of volume at the metal-ion site. Nevertheless, the overall properties of the SCO materials are determined by the amplitude of the intermolecular elastic interactions, which are responsible for what is traditionally called cooperativity. Noncovalent supramolecular interactions (host−guest, hydrogen bonding, $\pi-\pi$ interactions, etc.) are well known to bring mechanical elasticity to the network to propagate the local volume change of the molecule through the material. When the cooperativity is large enough, the spin-crossover can therefore be accompanied by a phase transition (also called a spin transition). However, effective control of the SCO properties remains a challenge due to the uncertainties in crystal engineering.

To meet this challenge, metal-ion dilution in SCO materials appears to be an appealing and straightforward synthetic strategy to control the propagation of elastic interactions between metallic centers.[12−15] Introducing inactive metal ions (i.e., non-SCO metal ions) in an SCO material separates the active centers and has for direct effect to modulate the volume change propagation and to tune the cooperativity. Besides, dilution of the active metal ion allows the tuning of the SCO temperature, $T_{1/2}$, in a nearly predictable manner by changing the internal pressure of the material.[16,17] A downward shift of $T_{1/2}$ in Fe^{II}-based SCO materials is expected upon substitution with ions of a similar or larger ionic radius than those of HS Fe^{II} (92 pm), such as Zn^{II} (88 pm), HS Mn^{II} (97 pm), HS Co^{II} (88.5 pm), and Cd^{II} (109 pm) ions.[18] In the case of Ni^{II} dilution, only a small effect on $T_{1/2}$ was observed since its radius (83 pm) lies halfway between HS Fe^{II} (92 pm) and LS Fe^{II} (75 pm).[18] But so far, metal-ion dilution was reported to have only a limited effect on tuning the SCO temperature (indeed decreasing it, in the absence of suitable metal ion with radius < 83 pm) at the cost of losing cooperativity.[19]

In 2019, we reported a mononuclear Fe^{II} complex, $[Fe(^{2Me}L)(NCBH_3)_2]$ (^{2Me}L = *N,N′*-dimethyl-*N,N′*-bis(2-pyridylmethyl)-1,2-ethanediamine), which exhibits an extremely slow dynamics of the spin transition process.[20] A full relaxation from the metastable high-spin state to the low-spin ground

state takes at least 3.7 h at 74−75 K. Identifying the microscopic mechanisms of this unusual dynamics, and even more, finding a way to control it, are essential to guide the design of new SCO materials with premeditated physical properties. Therefore, we oriented our investigations toward studying the metal dilution effects on the SCO dynamics of this unique system. Ni^{II} (83 pm) and Zn^{II} (88 pm) ions have been chosen as two representative metal ions considering their relative ionic radius in comparison to Fe^{II} (LS: 75 pm; HS: 92 pm). Herein, we demonstrate that the dynamics of the HS-to-LS transition can be blocked or accelerated by selecting the right metal ion for dilution.

RESULTS AND DISCUSSION

Synthesis and Structural Characterization. Three mixed-metal materials containing around 50% of Fe^{II}, $[Fe_xM_{1-x}(^{2Me}L)(NCBH_3)_2]$ (**$Fe_{0.52}Zn_{0.48}$**, **$Fe_{0.48}Ni_{0.52}$**, **$Fe_{0.41}Ni_{0.59}$**), were chosen to illustrate the metal dilution effects on the SCO dynamics. They were obtained using the same synthetic method as for the pristine Fe^{II} complex.[20] The metal fractions, x, as indicated in the name codes, were modulated by using different starting metal salts and were determined by inductively coupled plasma atomic emission spectroscopy (ICP-AES). Scanning electron microscopy−energy-dispersive spectroscopy (SEM-EDS) analysis confirmed that the two types of metal ions were uniformly distributed over the materials (Figure S1). The pure Ni^{II} and Zn^{II} compounds were also synthesized for comparison (see the Experimental Section). Single-crystal structures of all of the complexes were determined at 123 K and found to be isostructural to the pure Fe^{II} complex (monoclinic $C2/c$ space group).[20] The crystallographic data and refinement parameters are summarized in Tables S1 and S2. The metal ions are located in a distorted octahedral coordination sphere (Figure S2 and Table S2), composed of six N atoms from one tetradentate ^{2Me}L ligand and two $NCBH_3^-$ anions. The average metal−nitrogen distances in the pure $[M(^{2Me}L)(NCBH_3)_2]$ compounds are in line with the ionic radius of the metal ions, decreasing from 2.19 Å for HS Fe^{II}, 2.17 Å for Zn^{II}, 2.10 Å for Ni^{II}, down to 2.01 Å for LS Fe^{II}.[20] In **$Fe_{0.52}Zn_{0.48}$**, the average M−N distance of 2.18 Å is right in between the pure Zn^{II} and HS Fe^{II} compounds. In contrast, the average metal−nitrogen bond lengths in **$Fe_{0.41}Ni_{0.59}$** and **$Fe_{0.48}Ni_{0.52}$** (2.17 and 2.18 Å, respectively) are only slightly smaller than for the HS Fe complex. Overall, the bond length analysis in the three solid solutions indicates that Fe^{II} ions are all in their HS state at 123 K. Their crystal packing and intermolecular contacts are subject to only subtle changes compared to the pure Fe^{II} complex in its HS phase,[20] as confirmed by the Hirshfeld surface analysis (Figures S3 and S4). The predominant intermolecular interactions are found to be $\pi\cdots\pi$ interactions (Figures 1 and S4; Table S3; centroid−centroid distance ∼3.6 Å) and short contacts between B and H atoms from pyridine groups (∼0.2 Å shorter than the sum of van der Waals radii, Figure S5; Table S3). The short contacts observed in the LS phase of the pure Fe^{II} complex between C atoms from cyanoborohydride and H atoms from ethylene groups are absent in these mixed-metal structures.

Magnetic Properties. The magnetic susceptibility, χ, of the materials described in this work was measured on polycrystalline samples between 1.85 and 300 K. While the Zn^{II} complex is diamagnetic, the Ni^{II} complex is an $S = 1$ paramagnetic species with a χT product constant at 1.21 cm^3 K mol^{-1} between 20 and 300 K (Figure S6). The results for the mixed-metal materials are shown in Figure 2 in the form of χT versus T plots. Very different magnetic behaviors are observed, highlighting the major effects of the diluting metal ions on the SCO properties. The χT products at 300 K for **$Fe_{0.41}Ni_{0.59}$** (2.23 cm^3 K mol^{-1}), **$Fe_{0.48}Ni_{0.52}$** (2.58 cm^3 K mol^{-1}), and **$Fe_{0.52}Zn_{0.48}$** (2.40 cm^3 K mol^{-1}) are consistent with the sum of the fractional contributions from the pure complexes, i.e., 2.40, 2.61, and 2.14 cm^3 K mol^{-1} for **$Fe_{0.41}Ni_{0.59}$**, **$Fe_{0.48}Ni_{0.52}$**, **$Fe_{0.52}Zn_{0.48}$**, respectively. These values are estimated from the following relation $\chi T \approx x[\chi^{Fe}T]_{HS,300\ K} + (1-x)[\chi^{Zn/Ni}T]_{300\ K}$, where x is the fraction of the Fe^{II} ions determined by ICP-AES and $[\chi^{M}T]_{300\ K}$ is the value of the χT product for the pure complexes at 300 K (see the Experimental Section). These results confirm the presence of Fe^{II} ions in their HS state in all of these mixed-metal compounds.

In contrast to the pure Fe^{II} complex, for which its LS state is only accessible after more than 3.7 h of relaxation below 80 K,[20] the two Ni^{II}/Fe^{II} complexes show a clear spin-crossover between 90 and 50 K. With only 48% of Fe^{II} sites, **$Fe_{0.48}Ni_{0.52}$** nevertheless shows a 6 K thermal hysteresis (at 0.65 K min^{-1}; Figures 2 and S7) centered at 72 K and a rapid decay of the χT value between 85 and 50 K (with characteristic times of the order of a few minutes; Figure S7) as usually seen for SCO complexes. Lowering slightly the Fe^{II} concentration, **$Fe_{0.41}Ni_{0.59}$** displays a reversible spin crossover at 73 K without thermal hysteresis, proving that the Ni^{II} amount is an efficient tool for chemists to control the SCO dynamics in this system. At 20 K, the χT products are 1.06 and 1.15 cm^3 mol^{-1} K for **$Fe_{0.41}Ni_{0.59}$** and **$Fe_{0.48}Ni_{0.52}$**, respectively. As $\chi T > (1 -$

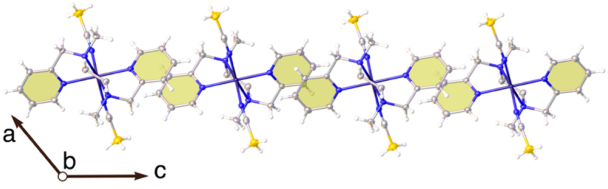

Figure 1. Single-crystal structure of **$Fe_{0.48}Ni_{0.52}$** and its 1D supramolecular arrangement generated by $\pi\cdots\pi$ interactions (at 123 K, 50% probability thermal ellipsoids). Color code: metal ion, dark purple; N, blue; C, gray; B, yellow; H, light gray.

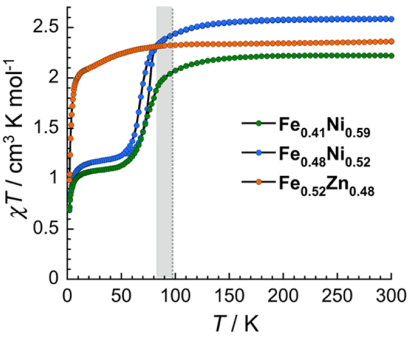

Figure 2. Temperature dependence of the χT products (χ being the dc magnetic susceptibility defined as M/H per mole of complex) at 1 T for **$Fe_{0.41}Ni_{0.59}$**, **$Fe_{0.48}Ni_{0.52}$**, and **$Fe_{0.52}Zn_{0.48}$** at a scan rate of 0.65 K min^{-1}. For comparison, the SCO signature of the pure $[Fe(^{2Me}L)(NCBH_3)_2]$ complex is shown by the gray zone and dotted gray vertical line, which indicates the supposed temperature domain of the thermal hysteresis and its highest temperature limit, respectively.[20]

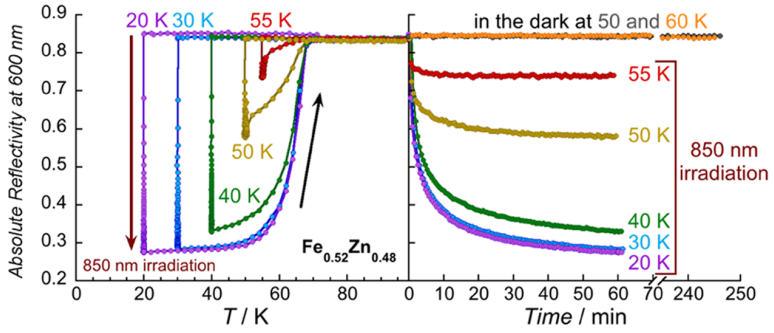

Figure 3. Left: Thermal variation of the 600 nm reflectivity signal in the dark (constant around 0.85 below 100 K) and after irradiation at 850 nm (2 mW cm^{-2}) at different temperatures for $\mathbf{Fe_{0.52}Zn_{0.48}}$. Right: Time evolution of the 600 nm signal in the dark (50 and 60 K) and during 850 nm irradiations (55−20 K; 2 mW cm^{-2}) at different temperatures (reached in the dark at 4 K min^{-1}).

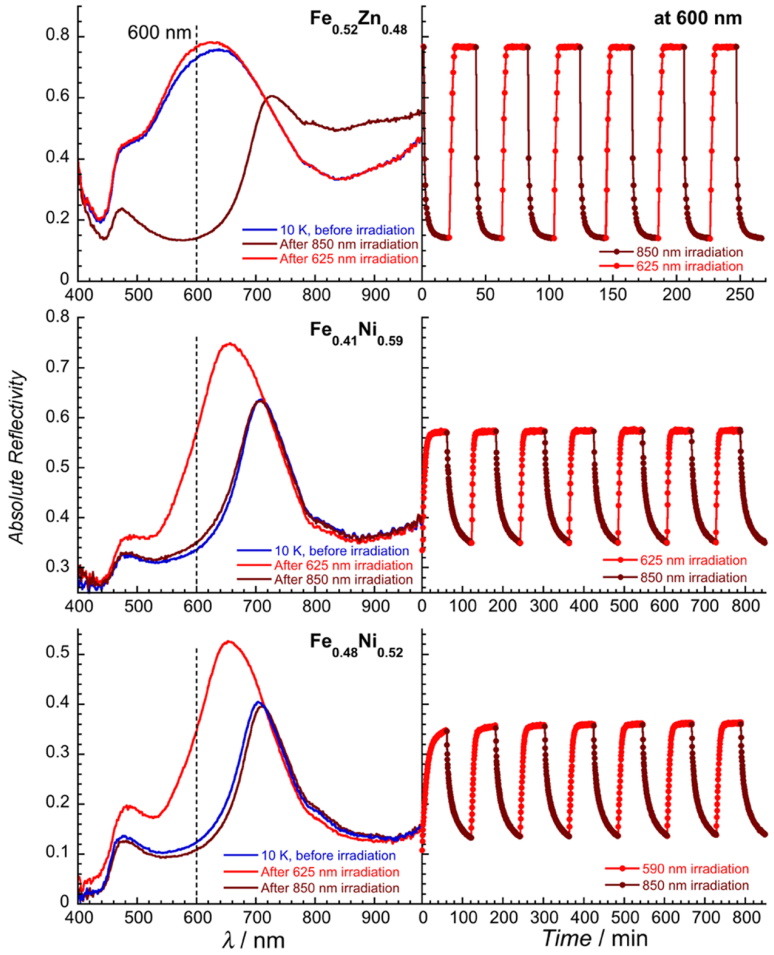

Figure 4. Left: Comparison of the optical reflectivity spectra at 10 K before any irradiation (blue), after successive 1 h irradiations at 850 nm (brown) and 625 nm (red) for $\mathbf{Fe_{0.52}Zn_{0.48}}$ (10 mW cm^{-2}), $\mathbf{Fe_{0.41}Ni_{0.59}}$ (2 mW cm^{-2}), and $\mathbf{Fe_{0.48}Ni_{0.52}}$ (5 mW cm^{-2}). Right: Time evolution of the 10 K reflectivity recorded at 600 nm during successive 590/625 nm (red) and 850 nm (brown) irradiations, showing the good reversibility and selectivity of the photoswitching for $\mathbf{Fe_{0.52}Zn_{0.48}}$ (2 mW cm^{-2}), $\mathbf{Fe_{0.41}Ni_{0.59}}$ (2 mW cm^{-2}), and $\mathbf{Fe_{0.48}Ni_{0.52}}$ (4 mW cm^{-2}).

$x)[\chi^{Ni}T]_{20\ K}$, these values include contributions from both S = 1 Ni^{II} and residual HS S = 2 Fe^{II} centers indicating (i) an incomplete HS-to-LS conversion and (ii) the following 20 K composition of the mixed-metal materials: $\mathbf{Fe_{HS,0.09}Fe_{LS,0.32}Ni_{0.59}}$ and $\mathbf{Fe_{HS,0.13}Fe_{LS,0.35}Ni_{0.52}}$ (to compare with $\mathbf{Fe_{HS,0.04}Fe_{LS,0.96}}$ for the pure Fe complex).[20] In these materials, the larger HS Fe^{II} residual below the SCO, i.e., the destabilization of the LS Fe^{II} ground state, is likely correlated to the presence of Ni^{II} metal ions, as the Ni^{II} radius lies nearly halfway between HS Fe^{II} and LS Fe^{II} ions. On the other hand, further decrease of the χT product below 15 K can be attributed to the intrinsic magnetic anisotropy of Ni^{II} and HS Fe^{II} sites, as already observed in the pure analogues (Figure S6).[20] In the case of the Zn^{II}/Fe^{II} material, $\mathbf{Fe_{0.52}Zn_{0.48}}$, the

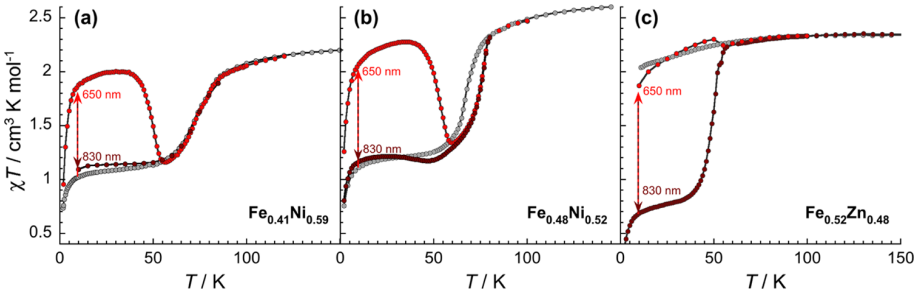

Figure 5. Temperature dependence of the χT product (measured in the dark and at 0.4 K min^{-1}) for $\mathbf{Fe_{0.41}Ni_{0.59}}$ (a; 0.1 T), $\mathbf{Fe_{0.48}Ni_{0.52}}$ (b; 0.1 T), and $\mathbf{Fe_{0.52}Zn_{0.48}}$ (c; 1 T) is shown in gray upon cooling down to 10 K. After cooling down the samples at 10 K in the dark, the red χT vs T data points were obtained after photoexcitation at 650 nm (at 10 mW cm^{-2}, 1 h) for $\mathbf{Fe_{0.41}Ni_{0.59}}$ (a) and $\mathbf{Fe_{0.48}Ni_{0.52}}$ (b), while for $\mathbf{Fe_{0.52}Zn_{0.48}}$ (c), successive photoexcitations at 830 nm (at 17 mW cm^{-2}, 7 h) and 650 nm (at 15 mW cm^{-2}, 30 min) were performed before the magnetic measurements. After cooling down the samples at 10 K in the dark, the brown χT vs T data points were obtained after photoexcitation at 830 nm (at 17 mW cm^{-2}, 5 h) for $\mathbf{Fe_{0.52}Zn_{0.48}}$ (c) while successive photoexcitations at 650 nm (at 10 W cm^{-2}, 1 h) and at 830 nm for $\mathbf{Fe_{0.41}Ni_{0.59}}$ (a; at 10 mW cm^{-2} during 2 h) and for $\mathbf{Fe_{0.48}Ni_{0.52}}$ (b; at 17 mW cm^{-2} during 5 h) were performed before the magnetic measurements.

SCO is completely suppressed, and only the paramagnetic behavior of the HS Fe^{II} metal ions is observed down to 1.85 K. Attempts to monitor the decay of the magnetization between 90 and 60 K show that the χT product over 1 to 2 h remains constant supporting the absence of slow dynamics in contrast to the magnetization decay observed for the pure Fe^{II} complex.[20]

Optical Reflectivity. The mixed-metal materials and their electronic properties were also studied by optical reflectivity. The SCO process can be followed in the 500−700 nm region corresponding to MLCT and/or d−d transitions of LS Fe^{II} complexes.[21,22] The reflectivity technique is very sensitive to subtle changes at the sample surface, making it particularly useful for detecting an SCO hidden at the bulk level, as seen with the pure Fe^{II} complex.[20] Thermal variation of the optical reflectivity spectra was collected for the three solid solutions (Figures S8−S10) in order to probe their thermochromism. The reflectivity at 600 nm for $\mathbf{Fe_{0.41}Ni_{0.59}}$ and $\mathbf{Fe_{0.48}Ni_{0.52}}$ (Figures S8 and S9) shows a clear temperature dependence consistent with an SCO at the Fe^{II} sites already observed in the magnetic investigations (Figure 2). On the other hand, the optical reflectivity data for $\mathbf{Fe_{0.52}Zn_{0.48}}$ (Figure S10) are not temperature-dependent, confirming that the SCO is suppressed in the Zn^{II}/Fe^{II} solid solution even at its surface. Moreover, as shown by the isothermal relaxation studies above 50 K (Figure 3), no sign of SCO with a slow dynamics was detected for $\mathbf{Fe_{0.52}Zn_{0.48}}$. Although the LS state of the Fe^{II} sites in $\mathbf{Fe_{0.52}Zn_{0.48}}$ is clearly not thermally accessible, an 850 nm irradiation below 55 K causes a light-induced HS-to-LS Fe^{II} conversion (Figures 3, 4, and S13).

The efficiency of the photoinduced HS-to-LS process increases with decreasing the excitation temperature as expected when a photoinduced metastable phase is generated and thermally trapped, being unable to relax to the thermodynamic ground state containing only HS Fe^{II} sites. Upon heating the sample, the photoinduced LS Fe^{II} sites relax fully to their HS state at 68 K (Figure 3). As shown in Figure 4 at 10 K, the HS Fe^{II} sites can also be recovered upon a 625 nm irradiation of the photo-generated LS centers (Figure 4). The LS and HS Fe^{II} sites in $\mathbf{Fe_{0.52}Zn_{0.48}}$ can thus be reversibly and efficiently addressed by 850 and 625 nm irradiations over several cycles without obvious fatigue. The optical reflectivity data also confirmed the good reversibility and selectivity of SCO photoswitching in the Fe^{II}/Ni^{II} solid solutions at 10 K (using 590 or 625 nm for the LS-to-HS conversion, and 850 nm for the HS-to-LS one; Figures 4, S11, and S12).

Photomagnetic Properties. The photomagnetic properties of $\mathbf{Fe_{0.41}Ni_{0.59}}$, $\mathbf{Fe_{0.48}Ni_{0.52}}$, and $\mathbf{Fe_{0.52}Zn_{0.48}}$ (Figure 5) were studied on polycrystalline samples at 10 K to test the photoswitchability of the SCO process at the bulk level. The samples were first cooled down to 10 K in the dark (gray data in Figure 5). Upon continuous 650 nm irradiation, the χT product of the two Ni^{II}/Fe^{II} solid solutions increases with time and reaches saturation at 1.86 and 2.05 cm^3 K mol^{-1} for $\mathbf{Fe_{0.41}Ni_{0.59}}$ and $\mathbf{Fe_{0.48}Ni_{0.52}}$, respectively. These values are consistent with a complete photoinduced population of the metastable HS state of the Fe^{II} sites. Subsequent 830 nm irradiation induces a decrease of the χT product down to a value that is only slightly higher (by about 5%) than the one obtained upon cooling in the dark (brown data in Figure 5). Upon heating in the dark, 650 nm photoinduced HS sites relax to the thermodynamic state at 55 K for $\mathbf{Fe_{0.41}Ni_{0.59}}$ and 58 K for $\mathbf{Fe_{0.48}Ni_{0.52}}$ (red data in Figure 5).

The bidirectional photoswitching of the SCO process is also observed for $\mathbf{Fe_{0.52}Zn_{0.48}}$. Upon 830 nm irradiation at 10 K, the χT product decreases to 0.68 cm^3 K mol^{-1}, indicating that ca. 60% of the Fe_{HS}^{II} centers are photoconverted to Fe_{LS}^{II}, leading to the following 10 K composition, $\mathbf{Fe_{HS,0.16}Fe_{LS,0.36}Zn_{0.48}}$. Reversibly, the LS-to-HS conversion of the Fe_{LS}^{II} sites can be quantitatively achieved upon 650 nm irradiation (red data in Figure 5). When increasing the temperature, the 830 nm photoinduced LS phase relaxes to the $\mathbf{Fe_{HS,0.52}Zn_{0.48}}$ phase at 56 K (brown data in Figure 5), which is similar to the relaxation of the photoinduced HS phase in $\mathbf{Fe_{0.41}Ni_{0.59}}$ (55 K) and $\mathbf{Fe_{0.48}Ni_{0.52}}$ (58 K) and contrasts with the relaxation observed around 95 K in the pure Fe complex. This result confirms the optical reflectivity study and the stabilization of the Fe_{HS}^{II} sites upon Zn dilution.

Discussion. The unusually slow dynamics of the spin transition in the pure Fe complex[20] finds its origin in (i) the small energy separation between the LS ground state and the HS excited state (that induces an SCO at low temperature; $T_{1/2}$ < 100 K) and (ii) concomitantly a large energy barrier between them (compared to $k_BT_{1/2}$) that thermally traps the metastable HS state. A metal-ion dilution is expected to play on both energetic parameters. By varying both the internal pressure of the material and modulating the elastic interactions, a metal-ion dilution can potentially (i) change

the ground state if the LS-HS energy separation is small, like in the present case, and (ii) modify the energy barrier and thus the SCO dynamics. Indeed, the $\mathbf{Fe_{0.52}Zn_{0.48}}$ solid solution gives the first experimental evidence that a controlled dilution can energetically switch the LS and HS states, leading to Fe^{II} sites with an HS ground state, which are still fully and reversibly photo-switchable (Figures 3–5). This unprecedented effect, which suppresses the thermal SCO process, is a direct consequence of the metal ion choice and the fact that Zn^{II} and HS Fe^{II} metal ions possess a similar ionic radius (88 vs 92 pm). The reversible photoswitchability of HS Fe^{II} sites observed in $\mathbf{Fe_{0.52}Zn_{0.48}}$ has only been observed in a few Fe^{II} coordination networks[23−27] and one Fe^{III} complex[28] for which the LS was a thermally hidden but still an accessible state. When diluted with Ni^{II}, which possesses an ionic radius (83 pm) intermediate between LS and HS Fe^{II} (75 vs 92 pm), the Fe^{II} centers in $\mathbf{Fe_{0.41}Ni_{0.59}}$ and $\mathbf{Fe_{0.48}Ni_{0.52}}$ possess an LS ground state like in the original $[Fe(^{2Me}L)(NCBH_3)_2]$ complex, but the energy separation with the HS excited state is reduced as illustrated by the decrease of $T_{1/2}$ (73−72 K vs 85−95 K). This $T_{1/2}$ shift to lower temperatures is relatively well known in the literature, as shown in Figure S14.[29−32] Indeed, a shift as high as ca. 90 K was reported for the $[Fe_xZn_{1-x}(bpp)_2](NCSe)_2$ solid solutions (bpp = 2,6-bis(pyrazol-3-yl)pyridine).[32] Simultaneously, the energy barrier governing the SCO dynamics is significantly reduced by the Ni^{II} dilution as demonstrated by direct observation of the thermal SCO by magnetic and optical measurements (Figures 2 and S7–S9), while it took at least 3.7 h for the pristine Fe complex.[20]

CONCLUSIONS

In conclusion, the $[Fe(^{2Me}L)(NCBH_3)_2]$ complex[20] was chosen in this work to illustrate how metal-ion dilutions can engender strong effects and some control on the thermodynamic and dynamic properties of an SCO material. In this particular system, the metal-ion substitution was expected to have more pronounced impacts due to its small LS/HS energy separation and its relatively large HS-to-LS energy barrier, which induce a spin-crossover at low temperatures with very slow dynamics. The dilution with Zn^{II} metal ions, which exhibit an ionic radius similar to the HS Fe^{II} centers, leads to the stabilization of the HS ground state at the Fe^{II} sites and, for the first time, a complete suppression of the thermally induced SCO process without destroying the reversible photoswitchability of the LS and HS states. When the Fe^{II} complexes are diluted by Ni^{II}, a smaller metal ion, the solid solutions preserve their LS ground state and photomagnetic activity with a lowering of $T_{1/2}$ (by about 20 K) and a faster SCO dynamics, implying a reduction of both LS/HS energy separation and HS-to-LS energy barrier. These successful chemical manipulations of the SCO process through controlled metal-ion dilutions open new synthetic strategies to design solid solutions with premeditated SCO properties. Future works are being developed in our laboratories to generalize this dilution approach with various stoichiometries, metal ions, and ligands in this system, as well as in a series of other SCO complexes.

EXPERIMENTAL SECTION

General Procedures. All reagents obtained from commercial sources were used without further purification. Safety Note: Perchlorate salts are potentially explosive, and caution should be taken when dealing with such materials.

Synthesis of $[M(^{2Me}L)(NCBH_3)_2]$ (M = Ni or Zn). To a solution of ^{2Me}L ligand (0.027 g, 0.1 mmol; ^{2Me}L = *N,N′*-dimethyl-*N,N′*-bis(2-pyridylmethyl)-1,2-ethanediamine) in methanol (15 mL) were added the metal salt ($NiCl_2{\cdot}6H_2O$ or $Zn(ClO_4)_2{\cdot}6H_2O$, 0.1 mmol) and $Na[NCBH_3]$ (0.013 g, 0.2 mmol). The resulting reaction mixture was stirred for 10 min, and the precipitate was filtered. Recrystallization from hot acetonitrile gave block crystals in ∼50% yield within a week. $[\mathbf{Ni}(^{2Me}\mathbf{L})(\mathbf{NCBH_3})_2]$, Elemental analysis calcd for $C_{18}H_{28}B_2N_6Ni$: C, 52.89; H, 6.90; N, 20.56. Found: C, 53.05; H, 6.85; N, 20.51. $[\mathbf{Zn}(^{2Me}\mathbf{L})(\mathbf{NCBH_3})_2]$, Elemental analysis calcd for $C_{18}H_{28}B_2N_6Zn$: C, 52.03; H, 6.79; N, 20.23. Found: C, 52.45; H, 6.65; N, 20.48.

Synthesis of the Mixed-Metal Materials, $[Fe_xM_{1-x}(^{2Me}L)(NCBH_3)_2]$ ($\mathbf{Fe_{0.41}Ni_{0.59}}$, $\mathbf{Fe_{0.48}Ni_{0.52}}$, $\mathbf{Fe_{0.52}Zn_{0.48}}$). The mixed-metal complexes were prepared in the same way as the pure materials, but using a mixture of metal salts in solution. The molar ratios of the metal salts were used as follows: Fe^{II}:Ni^{II} = 0.5:0.5 for $\mathbf{Fe_{0.41}Ni_{0.59}}$, Fe^{II}:Ni^{II} = 0.6:0.4 for $\mathbf{Fe_{0.48}Ni_{0.52}}$, and Fe^{II}:Zn^{II} = 0.5:0.5 for $\mathbf{Fe_{0.52}Zn_{0.48}}$. The single crystals were isolated in 50−60% yield within a week. The metal fractions in the final products were determined by inductively coupled plasma atomic emission spectroscopy (ICP-AES) and are indicated in the name codes. Elemental analysis for $\mathbf{Fe_{0.41}Ni_{0.59}}$, calcd for $C_{18}H_{28}B_2Fe_{0.41}N_6Ni_{0.59}$: C, 53.04; H, 6.92; N, 20.62. Found: C, 53.28; H, 6.86; N, 20.77. Elemental analysis for $\mathbf{Fe_{0.48}Ni_{0.52}}$, calcd for $C_{18}H_{28}B_2Fe_{0.48}N_6Ni_{0.52}$: C, 53.07; H, 6.93; N, 20.63. Found: C, 53.36; H, 6.91; N, 20.82. Elemental analysis for $\mathbf{Fe_{0.52}Zn_{0.48}}$, calcd for $C_{18}H_{28}B_2Fe_{0.52}N_6Zn_{0.48}$: C, 52.66; H, 6.87; N, 20.47. Found: C, 52.34; H, 6.69; N, 20.35. All of these Ni, Zn, and Fe-containing complexes show similar IR spectra (diamond ATR, cm^{-1}): 2348, 2329 (B-H), 2329, 2259, 2215, 2181(vs, C≡N), 1608, 1569, 1483, 1444, 1374, 1306, 1118(vs), 1060, 1020, 863, 822, 762(vs), 723.

Physical Characterization. Magnetic susceptibility measurements were recorded with a Quantum Design MPMS-XL SQUID magnetometer, operating with applied fields up to 7 T at temperatures from 1.85 to 300 K. Prior to the experiments, the field-dependent magnetization was measured at 100 K in order to detect the presence of any bulk ferromagnetic impurities. The samples appeared to be free of any significant ferromagnetic impurities. The photomagnetic experiments were performed using a set of photodiodes coupled via an optical fiber to the cavity of an MPMS-5S Quantum Design SQUID magnetometer. Samples were maintained in a straw between two thin layers of polyethylene films to limit orientation effects. Note that the temperatures have been corrected to consider the light irradiation heating (an average +2 K has been observed with red light). Experimental susceptibilities were corrected for sample holder and intrinsic diamagnetic contributions. The fraction of HS Fe^{II} ions, γ_{HS}, involved in the spin-crossover in the mixed-metal complexes was calculated according to the following equations

$$\chi T = x\chi^{Fe}T + (1-x)\chi^{M}T \quad (1)$$

$$\chi^{Fe}T = (\chi T - (1-x)\chi^{M}T)/x \quad (2)$$

$$\gamma_{HS} = \chi^{Fe}T/[\chi^{Fe}T]_{HS} \quad (3)$$

where x is the molar fraction of the Fe^{II} ions in the solid solution, $\chi^{M}T$ is the χT value of the pure metal complex; in a rough approximation, this value is set to be constant above 20 K: $\chi^{Ni}T \approx [\chi^{Ni}T]_{300\ K}$ = 1.21 $cm^3\ K\ mol^{-1}$, $\chi^{Zn}T$ = 0 $cm^3\ K\ mol^{-1}$ and $[\chi^{Fe}T]_{HS} = [\chi^{Fe}T]_{300\ K}$ = 4.12 $cm^3\ K\ mol^{-1}$.

Surface reflectivity measurements have been performed with a home-built system, operating between 10 and 300 K (at 4 K min^{-1}) and in a spectrometric range from 400 to 1000 nm. A halogen-tungsten light source (Leica CLS 150 XD tungsten halogen source adjustable from 0.05 mW cm^{-2} to 1 W cm^{-2}) was used as the spectroscopic light. The measurements were calibrated with barium sulfate as the reference sample. As the samples are potentially very photosensitive, the light exposure time was minimized during the experiments keeping the samples in the dark except during the

measurements when white light is shined on the sample surface (P = 0.08 mW cm^{-2}). For all of the excitation/de-excitation experiments performed at 10 K, the sample was initially placed at this temperature keeping the sample in the dark to avoid any excitation. For white light irradiation, the source described above was used but in a continuous manner with a power of 0.08 mW cm^{-2}. Light-emitting diodes (LEDs) operating between 365 and 1050 nm (from Thorlabs) were used for excitation experiments. For the excitation/de-excitation experiments in optical reflectivity and photomagnetism, the power and the time of the irradiation were systematically adapted to the optical properties of the materials in order to obtain the fastest possible response and to minimize thermal heating effects.

Elemental analyses were performed using an Elementar Vario EL Elemental Analyzer. Inductively coupled plasma atomic emission spectrometry analysis (ICP-AES) was carried out with a SPECTRO CIROS VISION emission spectrometer. IR spectra were recorded by the attenuated-total-reflectance (ATR) technique in the range 4000−650 cm^{-1} using a PerkinElmer spectrometer. The microstructures and the chemical composition were characterized using SEM (Hitachi Regulus 8100, Japan) equipped with an energy-dispersive X-ray spectrometer (EDS, Oxford Ultim Max 65, UK) operated at 20 kV. Hirshfeld surface analyses were performed with CrystalExplorer.[33]

Single-Crystal X-ray Diffraction. Single-crystal X-ray data were collected at 123 K with an Xcalibur, Eos, Gemini diffractometer, equipped with a graphite monochromator centered on the path of Cu Kα radiation (λ = 1.54184 Å). A multiscan absorption correction was performed. The structures were solved using the direct method (SHELXS) and refined by full-matrix least-squares on F^2 using SHELXL[34] under the graphical user interface of Olex2.[35]

CCDC 2143019−2143023 contain the supplementary crystallographic data for this paper. These data can be obtained free of charge via www.ccdc.cam.ac.uk/data_request/cif, or by emailing data_request@ccdc.cam.ac.uk, or by contacting The Cambridge Crystallographic Data Centre, 12 Union Road, Cambridge CB2 1EZ, UK; fax: +44 1223 336033.

AUTHOR INFORMATION

Corresponding Authors

Corine Mathonière − *Univ. Bordeaux, CNRS, CRPP, UMR 5031, F-33600 Pessac, France; Univ. Bordeaux, CNRS, Bordeaux INP, ICMCB, UMR 5026, F-33600 Pessac, France*; Email: corine.mathoniere@u-bordeaux.fr

Rodolphe Clérac − *Univ. Bordeaux, CNRS, CRPP, UMR 5031, F-33600 Pessac, France;* orcid.org/0000-0001-5429-7418; Email: rodolphe.clerac@u-bordeaux.fr

Xin Bao − *School of Chemistry and Chemical Engineering, Nanjing University of Science and Technology, Nanjing 210094, P. R. China;* orcid.org/0000-0002-2725-0195; Email: baox199@126.com

Authors

Xiang Li − *School of Chemistry and Chemical Engineering, Nanjing University of Science and Technology, Nanjing 210094, P. R. China*

Dong Zhang − *School of Chemistry and Chemical Engineering, Nanjing University of Science and Technology, Nanjing 210094, P. R. China*

Yuqing Qian − *School of Chemistry and Chemical Engineering, Nanjing University of Science and Technology, Nanjing 210094, P. R. China*

Wenxuan Liu − *School of Chemistry and Chemical Engineering, Nanjing University of Science and Technology, Nanjing 210094, P. R. China*

ACKNOWLEDGMENTS

This work was supported by the National Natural Science Foundation of China (22175092) and the Fundamental Research Funds for the Central Universities, No. 30922010602. X.B., C.M., and R.C. thank the Nanjing University of Science and Technology for financially supporting this collaborative research program. C.M. and R.C. thank the University of Bordeaux, the Région Nouvelle Aquitaine, Quantum Matter Bordeaux (QMBx), the Centre National de la Recherche Scientifique (CNRS), and the Association Française de Magnétisme Moléculaire.

REFERENCES

(1) Murray, K. S. The Development of Spin-Crossover Research. In *Spin-Crossover Materials: Properties and Applications*; Halcrow, M. A., Ed.; John Wiley & Sons Ltd: Oxford, UK, 2013; pp 1−54.

(2) Létard, J.-F.; Guionneau, P.; Goux-Capes, L. Towards Spin Crossover Applications. In *Spin Crossover in Transition Metal Compounds III*; Springer-Verlag: Berlin/Heidelberg, 2004; Vol. *1*, pp 221−249.

(3) Feng, M.; Ruan, Z.-Y.; Chen, Y.-C.; Tong, M.-L. Physical Stimulus and Chemical Modulations of Bistable Molecular Magnetic Materials. *Chem. Commun.* **2020**, *56*, 13702−13718.

(4) Sato, O. Dynamic Molecular Crystals with Switchable Physical Properties. *Nat. Chem.* **2016**, *8*, 644−656.

(5) Hogue, R. W.; Singh, S.; Brooker, S. Spin Crossover in Discrete Polynuclear Iron(II) Complexes. *Chem. Soc. Rev.* **2018**, *47*, 7303−7338.

(6) Kumar, K. S.; Ruben, M. Sublimable Spin-Crossover Complexes: From Spin-State Switching to Molecular Devices. *Angew. Chem., Int. Ed.* **2021**, *60*, 7502−7521.

(7) Kumar, K. S.; Ruben, M. Emerging Trends in Spin Crossover (SCO) Based Functional Materials and Devices. *Coord. Chem. Rev.* **2017**, *346*, 176−205.

(8) Coronado, E. Molecular Magnetism: From Chemical Design to Spin Control in Molecules, Materials and Devices. *Nat. Rev. Mater.* **2020**, *5*, 87−104.

(9) Rubio-Giménez, V.; Tatay, S.; Martí-Gastaldo, C. Electrical Conductivity and Magnetic Bistability in Metal-Organic Frameworks and Coordination Polymers: Charge Transport and Spin Crossover at the Nanoscale. *Chem. Soc. Rev.* **2020**, *49*, 5601−5638.

(10) Molnár, G.; Rat, S.; Salmon, L.; Nicolazzi, W.; Bousseksou, A. Spin Crossover Nanomaterials: From Fundamental Concepts to Devices. *Adv. Mater.* **2018**, *30*, No. 1703862.

(11) Wang, H.-Y.; Ge, J.-Y.; Hua, C.; Jiao, C.-Q.; Wu, Y.; Leong, C. F.; D'Alessandro, D. M.; Liu, T.; Zuo, J.-L. Photo- and Electronically Switchable Spin-Crossover Iron(II) Metal-Organic Frameworks Based on a Tetrathiafulvalene Ligand. *Angew. Chem., Int. Ed.* **2017**, *56*, 5465−5470.

(12) Tayagaki, T.; Galet, A.; Molnár, G.; Muñoz, M. C.; Zwick, A.; Tanaka, K.; Real, J.-A.; Bousseksou, A. Metal Dilution Effects on the

Spin-Crossover Properties of the Three-Dimensional Coordination Polymer Fe(Pyrazine)[Pt(CN)$_4$]. *J. Phys. Chem. B* **2005**, *109*, 14859−14867.
(13) Spiering, H. Elastic Interaction in Spin-Crossover Compounds. In *Spin Crossover in Transition Metal Compounds III*; Springer-Verlag: Berlin/Heidelberg, 2006; pp 171−195.
(14) Sorai, M.; Ensling, J.; Hasselbach, K. M.; Gütlich, P. Mössbauer Effect Study On The High-Spin ($^5T_2$) ⇌ Low-Spin ($^1A_1$) Transition in [Fe(2-Pic)$_3$]Cl$_2$. Dilution Effect in [Fe$_x$Zn$_{1-x}$(2-Pic)$_3$]Cl$_2$.EtOH and C. *J. Phys. Colloq.* **1976**, *37*, C6-479.
(15) König, E.; Ritter, G.; Kulshreshtha, S. K. The Nature of Spin-State Transitions in Solid Complexes of Iron(II) and the Interpretation of Some Associated Phenomena. *Chem. Rev.* **1985**, *85*, 219−234.
(16) Martin, J. P.; Zarembowitch, J.; Dworkin, A.; Haasnoot, J. G.; Codjovi, E. Solid-State Effects in Spin Transitions: Influence of Iron(II) Dilution on the Magnetic and Calorimetric Properties of the Series [Fe$_x$Ni$_{1-x}$(4,4′-Bis(1,2,4-Triazole))$_2$(NCS)$_2$]·H$_2$O. *Inorg. Chem.* **1994**, *33*, 2617−2623.
(17) Chakraborty, P.; Enachescu, C.; Hauser, A. Analysis of the Experimental Data for Pure and Diluted [Fe$_x$Zn$_{1-x}$(Bbtr)$_3$](ClO$_4$)$_2$ Spin-Crossover Solids in the Framework of a Mechanoelastic Model. *Eur. J. Inorg. Chem.* **2013**, *2013*, 770−780.
(18) Shannon, R. D. Revised Effective Ionic Radii and Systematic Studies of Interatomic Distances in Halides and Chalcogenides. *Acta Crystallogr., Sect. A* **1976**, *32*, 751−767.
(19) Sylla, M. S.; Baldé, C.; Daro, N.; Desplanches, C.; Marchivie, M.; Chastanet, G. On the Effect of the Internal Pressure on the Photoinduced Spin-Crossover Behavior of [Fe$_x$M$_{1-x}$(1,10-Phenanthroline)$_2$(NCS)$_2$] Solid Solutions (M = Ni^{II}, Zn^{II}, and Cd^{II}). *Eur. J. Inorg. Chem.* **2018**, *2018*, 297−304.
(20) Ye, Y. S.; Chen, X. Q.; De Cai, Y.; Fei, B.; Dechambenoit, P.; Rouzières, M.; Mathonière, C.; Clérac, R.; Bao, X. Slow Dynamics of the Spin-Crossover Process in an Apparent High-Spin Mononuclear Fe^{II} Complex. *Angew. Chem., Int. Ed.* **2019**, *58*, 18888−18891.
(21) Costa, J. S.; Lappalainen, K.; de Ruiter, G.; Quesada, M.; Tang, J.; Mutikainen, I.; Turpeinen, U.; Grunert, C. M.; Gütlich, P.; Lazar, H. Z.; Létard, J.-F.; Gamez, P.; Reedijk, J. Remarkable Steric Effects and Influence of Monodentate Axial Ligands L on the Spin-Crossover Properties of Trans-[Fe^{II}(N$_4$Ligand)L] Complexes. *Inorg. Chem.* **2007**, *46*, 4079−4089.
(22) Glijer, D.; Hébert, J.; Trzop, E.; Collet, E.; Toupet, L.; Cailleau, H.; Matouzenko, G. S.; Lazar, H. Z.; Létard, J. F.; Koshihara, S.; Buron-Le Cointe, M. Photoinduced Phenomena and Structural Analysis Associated with the Spin-State Switching in the [Fe^{II}(DPEA)(NCS)$_2$]. *Phys. Rev. B* **2008**, *78*, No. 134112.
(23) Chen, Y. C.; Meng, Y.; Dong, Y. J.; Song, X. W.; Huang, G. Z.; Zhang, C. L.; Ni, Z. P.; Navařík, J.; Malina, O.; Zbořil, R.; Tong, M.-L. Light- And Temperature-Assisted Spin State Annealing: Accessing the Hidden Multistability. *Chem. Sci.* **2020**, *11*, 3281−3289.
(24) Milin, E.; Patinec, V.; Triki, S.; Bendeif, E.-E.; Pillet, S.; Marchivie, M.; Chastanet, G.; Boukheddaden, K. Elastic Frustration Triggering Photoinduced Hidden Hysteresis and Multistability in a Two-Dimensional Photoswitchable Hofmann-Like Spin-Crossover Metal−Organic Framework. *Inorg. Chem.* **2016**, *55*, 11652−11661.
(25) Chakraborty, P.; Pillet, S.; Bendeif, E. E.; Enachescu, C.; Bronisz, R.; Hauser, A. Light-Induced Bistability in the 2D Coordination Network {[Fe(Bbtr)$_3$][BF$_4$]$_2$}$_\infty$: Wavelength-Selective Addressing of Molecular Spin States. *Chem. − Eur. J.* **2013**, *19*, 11418−11428.
(26) Ndiaye, M. M.; Pillet, S.; Bendeif, E. E.; Marchivie, M.; Chastanet, G.; Boukheddaden, K.; Triki, S. Hidden Hysteretic Behavior of a Paramagnetic Iron(II) Network Revealed by Light Irradiation. *Eur. J. Inorg. Chem.* **2018**, *2018*, 305−313.
(27) Chakraborty, P.; Bronisz, R.; Besnard, C.; Guénée, L.; Pattison, P.; Hauser, A. Persistent Bidirectional Optical Switching in the 2D High-Spin Polymer {[Fe(bbtr)$_3$](BF$_4$)$_2$}$_\infty$. *J. Am. Chem. Soc.* **2012**, *134*, 4049−4052.
(28) Boonprab, T.; Lee, S. J.; Telfer, S. G.; Murray, K. S.; Phonsri, W.; Chastanet, G.; Collet, E.; Trzop, E.; Jameson, G. N. L.; Harding, P.; Harding, D. J. The First Observation of Hidden Hysteresis in an Iron(III) Spin-Crossover Complex. *Angew. Chem., Int. Ed.* **2019**, *58*, 11811−11815.
(29) Baldé, C.; Desplanches, C.; Létard, J.-F.; Chastanet, G. Effects of Metal Dilution on the Spin-Crossover Behavior and Light Induced Bistability of Iron(II) in [Fe$_x$Ni$_{1-x}$(Bpp)$_2$](NCSe)$_2$. *Polyhedron* **2017**, *123*, 138−144.
(30) Chakraborty, P.; Enachescu, C.; Walder, C.; Bronisz, R.; Hauser, A. Thermal and Light-Induced Spin Switching Dynamics in the 2D Coordination Network of {[Zn$_{1-x}$Fe$_x$(Bbtr)$_3$](ClO$_4$)$_2$}$_\infty$: The Role of Cooperative Effects. *Inorg. Chem.* **2012**, *51*, 9714−9722.
(31) Baldé, C.; Desplanches, C.; Grunert, M.; Wei, Y.; Gütlich, P.; Létard, J. F. Influence of Metal Dilution on the Light-Induced Spin Transition in Two 1D Chain Compounds: [Fe$_x$Zn$_{1-x}$(Btzp)$_3$](BF$_4$)$_2$ and [Fe$_x$Zn$_{1-x}$(Endi)$_3$](BF$_4$)$_2$. *Eur. J. Inorg. Chem.* **2008**, *34*, 5382−5389.
(32) Baldé, C.; Desplanches, C.; Le Gac, F.; Guionneau, P.; Létard, J.-F. The Role of Iron(II) Dilution in the Magnetic and Photomagnetic Properties of the Series [Fe$_x$Zn$_{1-x}$(Bpp)$_2$](NCSe)$_2$. *Dalton Trans.* **2014**, *43*, 7820−7829.
(33) Turner, M.; McKinnon, J.; Wolff, S.; Grimwood, D.; Spackman, P.; Jayatilaka, D.; Spackman, M. *CrystalExplorer*, Ver. 17.5; University of Western Australia 2018.
(34) Sheldrick, G. M. A Short History of SHELX. *Acta Crystallogr., Sect. A: Found. Crystallogr.* **2008**, *64*, 112−122.
(35) Dolomanov, O. V.; Bourhis, L. J.; Gildea, R. J.; Howard, J. A. K.; Puschmann, H. OLEX2: A Complete Structure Solution, Refinement and Analysis Program. *J. Appl. Crystallogr.* **2009**, *42*, 339−341.

Chemical Manipulation of the Spin-Crossover Dynamics through Judicious Metal Ion Dilution

Xiang Li,[a] Dong Zhang,[a] Yuqing Qian,[a] Wenxuan Liu,[a] Corine Mathonière,[b,c,*] Rodolphe Clérac[b,*] and Xin Bao[a,*]

[a] School of Chemistry and Chemical Engineering, Nanjing University of Science and Technology, 210094 Nanjing, P. R. China.

[b] Univ. Bordeaux, CNRS, CRPP, UMR 5031, F-33600 Pessac, France.

[c] Univ. Bordeaux, CNRS, Bordeaux INP, ICMCB, UMR 5026, F-33600 Pessac, France.

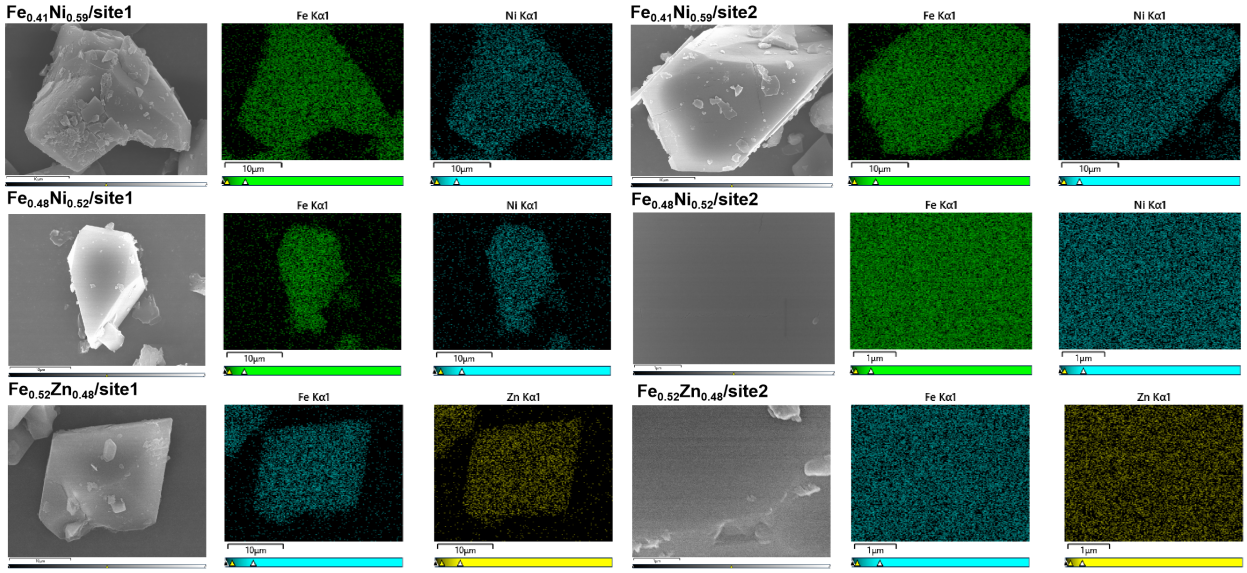

Figure S1. SEM-EDS mapping of **$Fe_{0.41}Ni_{0.59}$**, **$Fe_{0.48}Ni_{0.52}$** and **$Fe_{0.52}Zn_{0.48}$** crystals showing that the two types of metal ions are uniformly distributed over the materials.

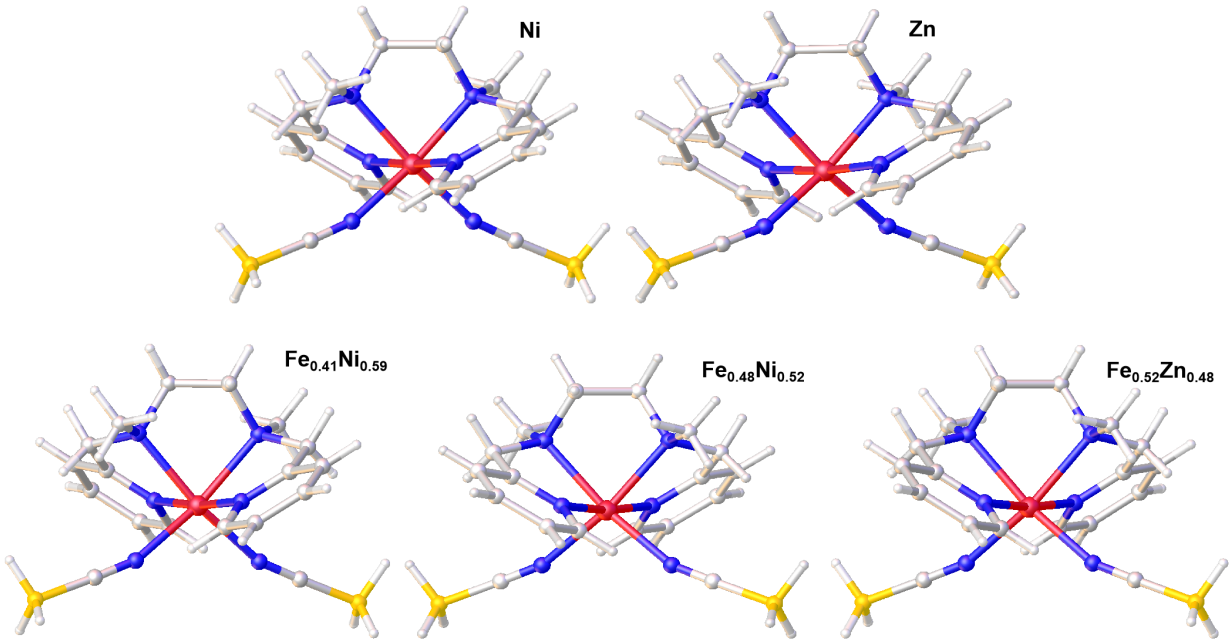

Figure S2. View of the molecular structure of the **Ni**, **Zn**, **$Fe_{0.41}Ni_{0.59}$**, **$Fe_{0.48}Ni_{0.52}$** and **$Fe_{0.52}Zn_{0.48}$** complexes from single-crystal X-ray diffraction at 123 K (see also Table S1 and S2). Color code: metal ion, red; N, blue, C, gray; B, yellow; H, light gray.

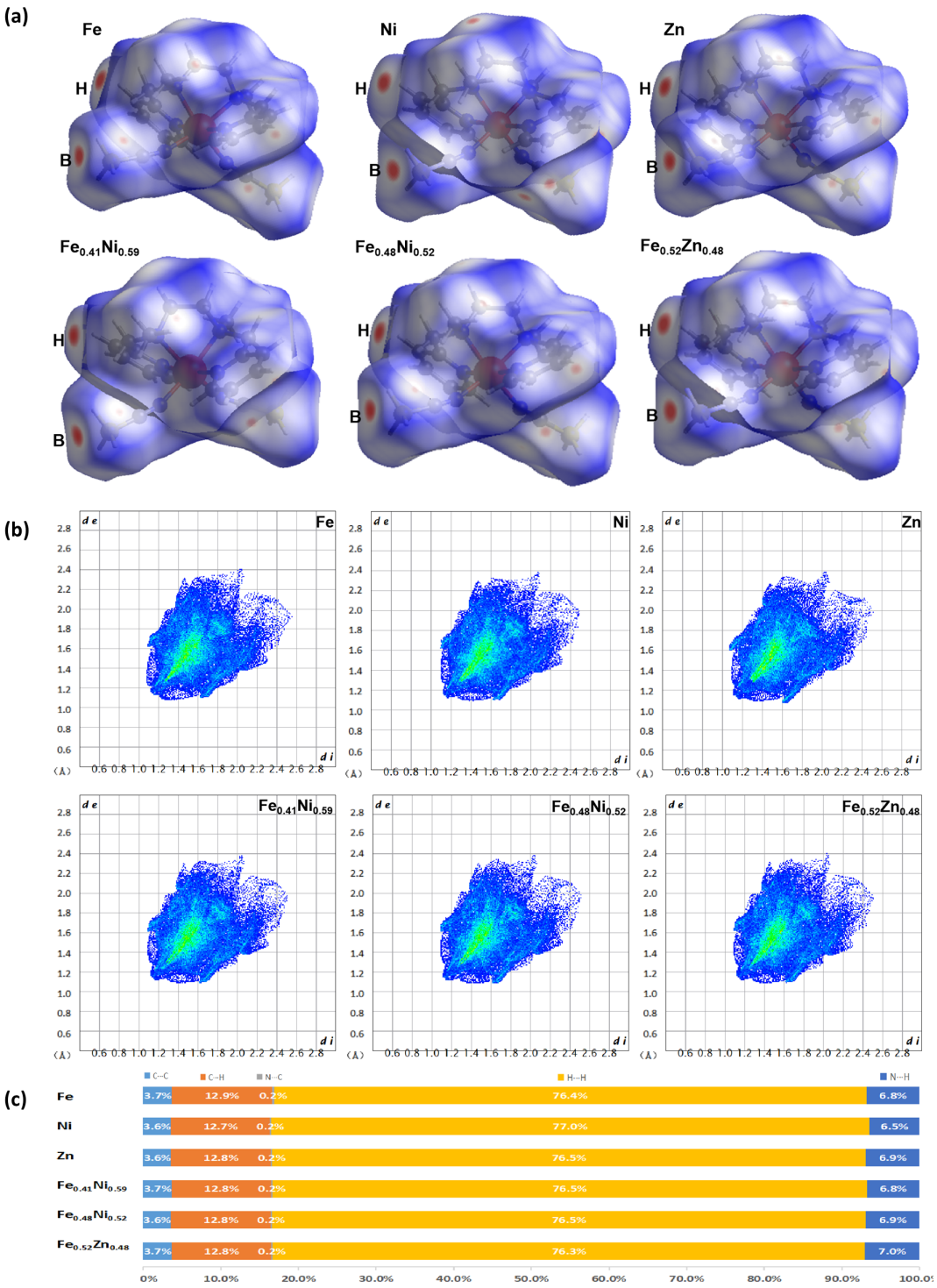

Figure S3. (a) Hirshfeld surfaces, (b) 2D fingerprint plots and (c) relative contributions to the Hirshfeld surface from various intermolecular contacts in the crystal packing at 123 K for the **Fe**, **Ni**, **Zn**, **$Fe_{0.41}Ni_{0.59}$**, **$Fe_{0.48}Ni_{0.52}$** and **$Fe_{0.52}Zn_{0.48}$** complexes. The crystal packing and intermolecular contacts for these complexes are very similar to the pure Fe^{II} complex in its HS phase.[1]

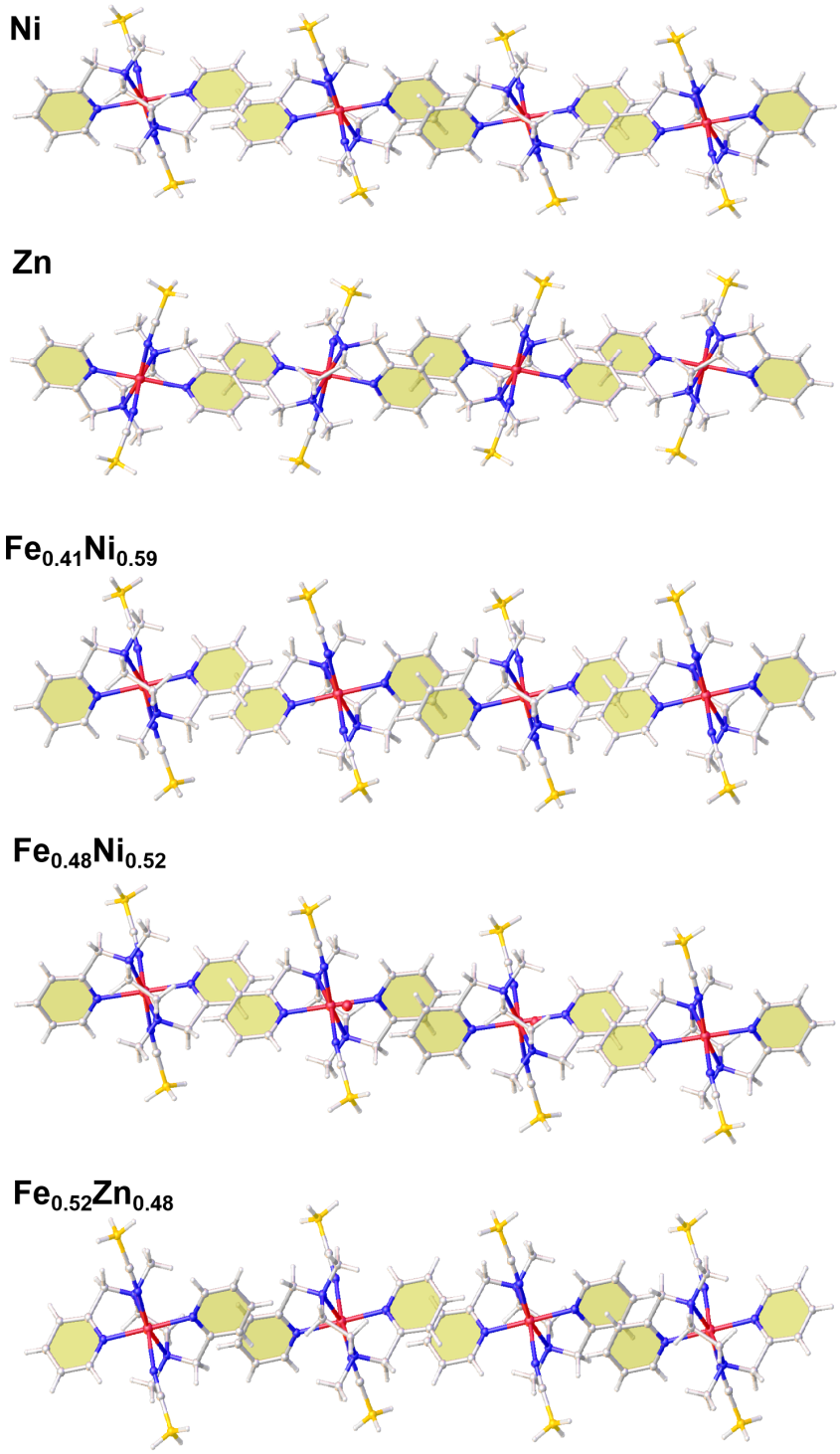

Figure S4. View of the 1D supramolecular arrangement generated by π···π interactions for the **Ni**, **Zn**, **$Fe_{0.41}Ni_{0.59}$**, **$Fe_{0.48}Ni_{0.52}$** and **$Fe_{0.52}Zn_{0.48}$** complexes obtained from single-crystal X-ray diffraction at 123 K. Color code: metal ion, red; N, blue, C, gray; B, yellow; H, light gray.

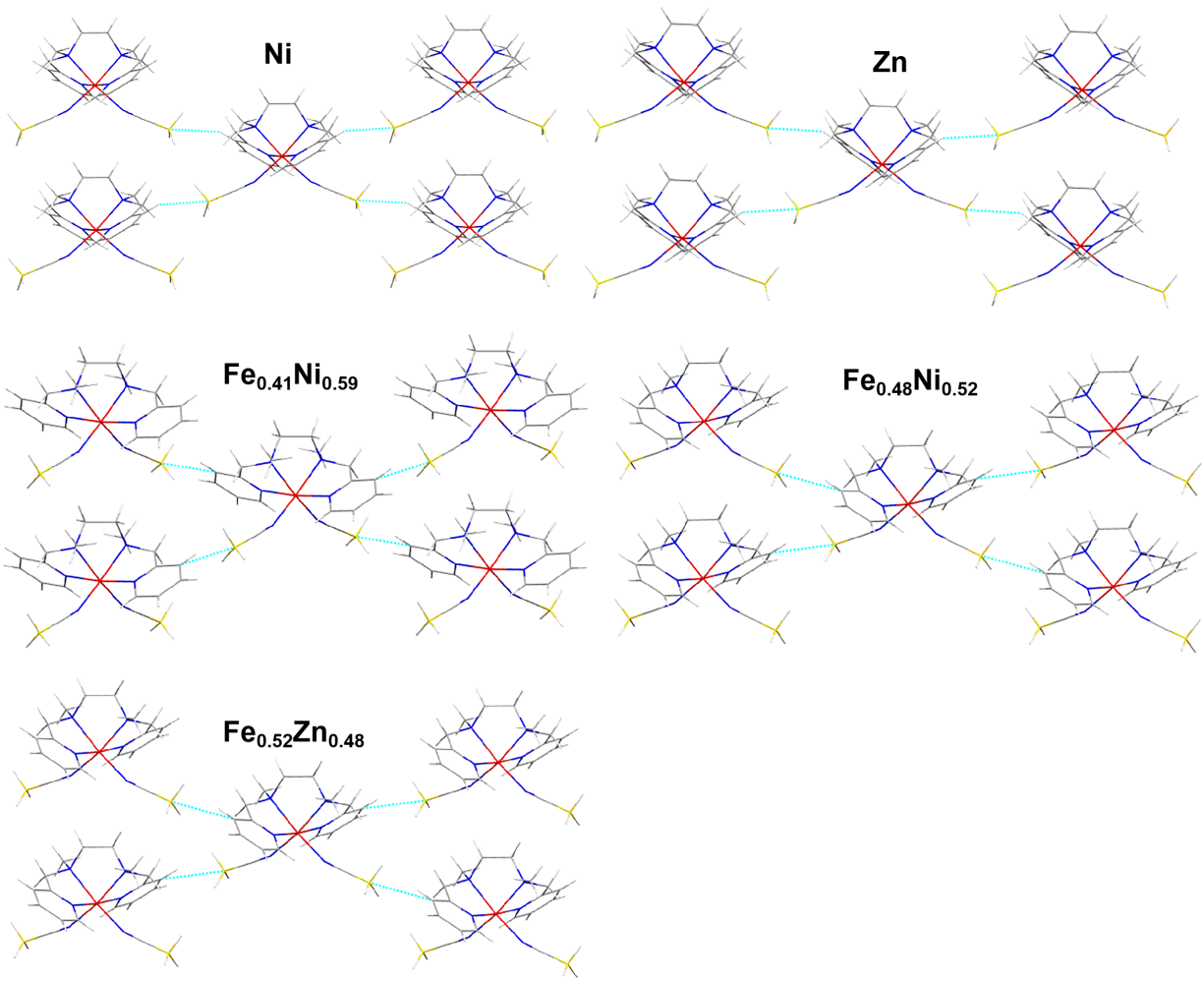

Figure S5. View of the crystal packing for the **Ni**, **Zn**, **$Fe_{0.41}Ni_{0.59}$**, **$Fe_{0.48}Ni_{0.52}$** and **$Fe_{0.52}Zn_{0.48}$** complexes (obtained from single-crystal X-ray diffraction at 123 K) showing the supramolecular interactions between B atoms and H atoms from the pyridine groups of the ^{2Me}L ligand in the (*ab*) plane (blue dotted lines). Color code: metal ion, red; N, blue, C, gray; B, yellow; H, light gray.

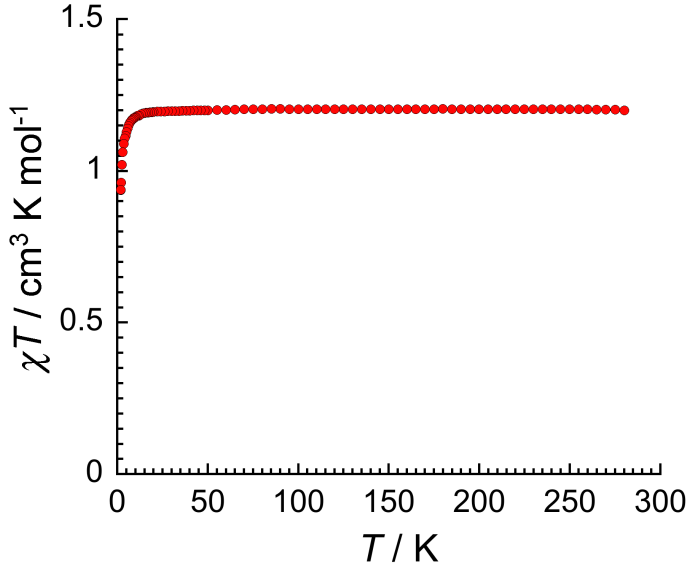

Figure S6. Temperature dependence of the χT product at 0.1 T for **[Ni(^{2Me}L)(NCBH$_3$)$_2$]** (χ is defined as M/H per mole of the complex) at 1.3 K/min.

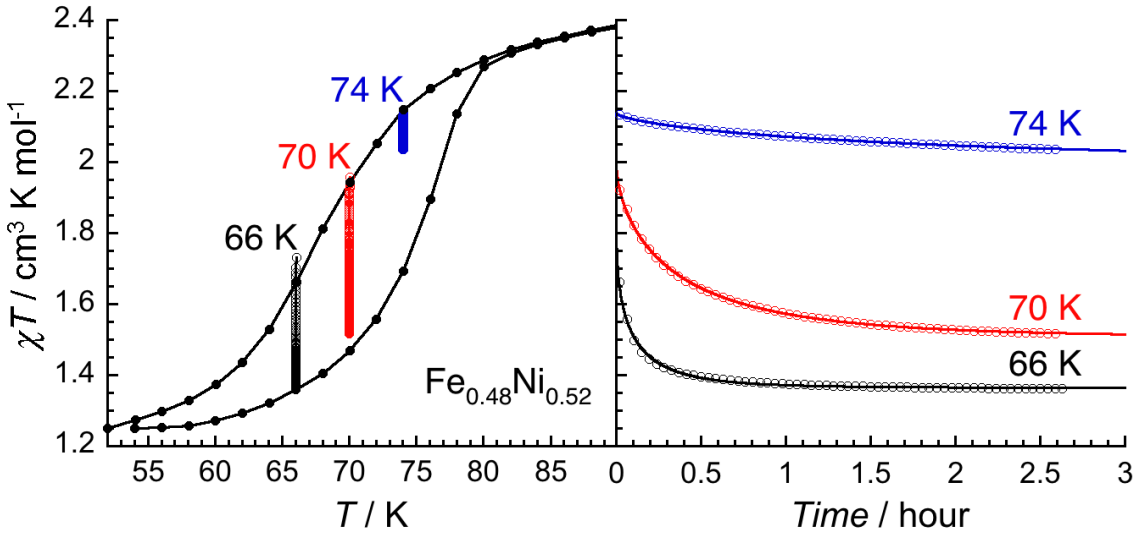

Figure S7. Temperature (left) and time (right) dependence of the χT product at 1 T for **Fe$_{0.48}$Ni$_{0.52}$** zoomed in the thermal hysteresis region. The solid line is inserted to guide the eye on the left part of the figure and the black vertical lines show the isothermal relaxations at 74, 70 and 66 K (see right part). On the right part of the figure, the experimental decay of the χT product were fitted to stretched exponential functions with a characteristic time of 5.7, 22 and 116 minutes at 66, 70 and 74 K, respectively.

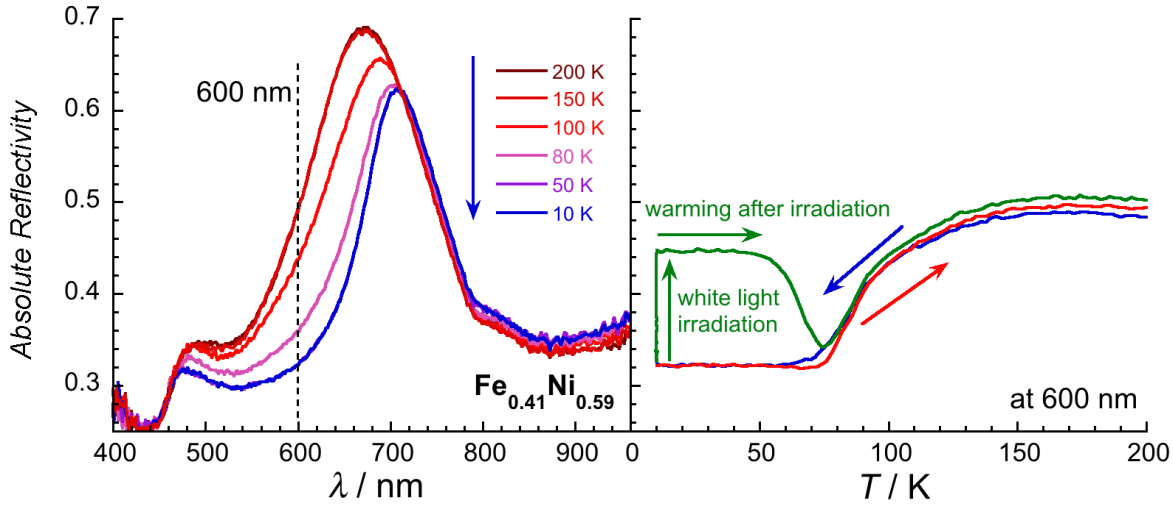

Figure S8. Left: Selected optical reflectivity spectra for $Fe_{0.41}Ni_{0.59}$ between 200 and 10 K recorded in the dark in cooling mode and at a scan rate of 4 K min^{-1}. Right: Thermal variation of the 600-nm optical reflectivity signal recorded at a scan rate of 4 K min^{-1} when cooling (blue trace) and heating (red trace) in the dark and when heating (green trace) after white light irradiation at 10 K. A spectroscopic white light of 0.08 mW cm^{-2} has been used for these measurements.

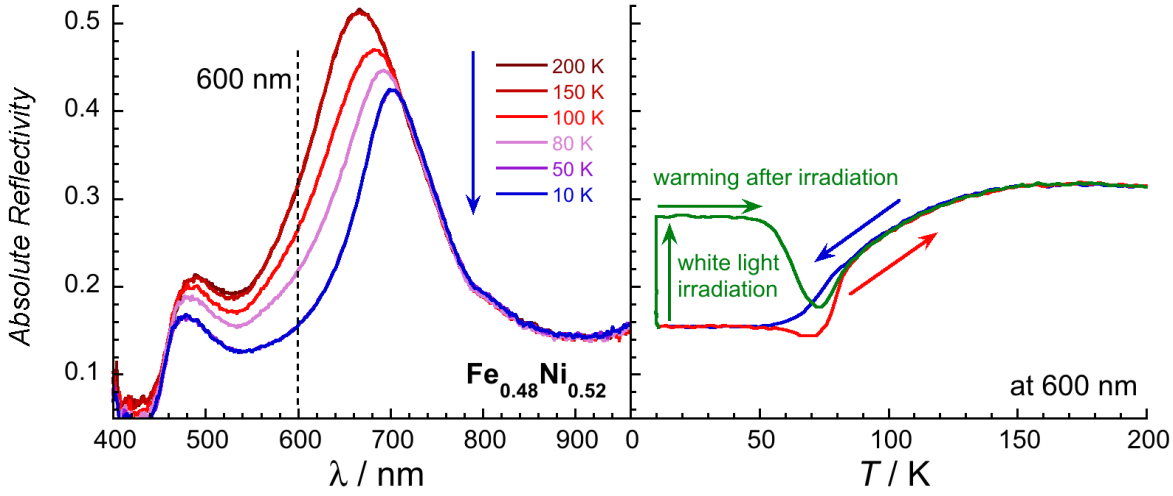

Figure S9. Left: Selected optical reflectivity spectra for $Fe_{0.48}Ni_{0.52}$ between 200 and 10 K recorded in the dark in cooling mode and at a scan rate of 4 K min^{-1}. Right: Thermal variation of the 600-nm optical reflectivity signal recorded at a scan rate of 4 K min^{-1} when cooling (blue trace) and heating (red trace) in the dark and when heating (green trace) after white light irradiation at 10 K. A spectroscopic white light of 0.08 mW cm^{-2} has been used for these measurements.

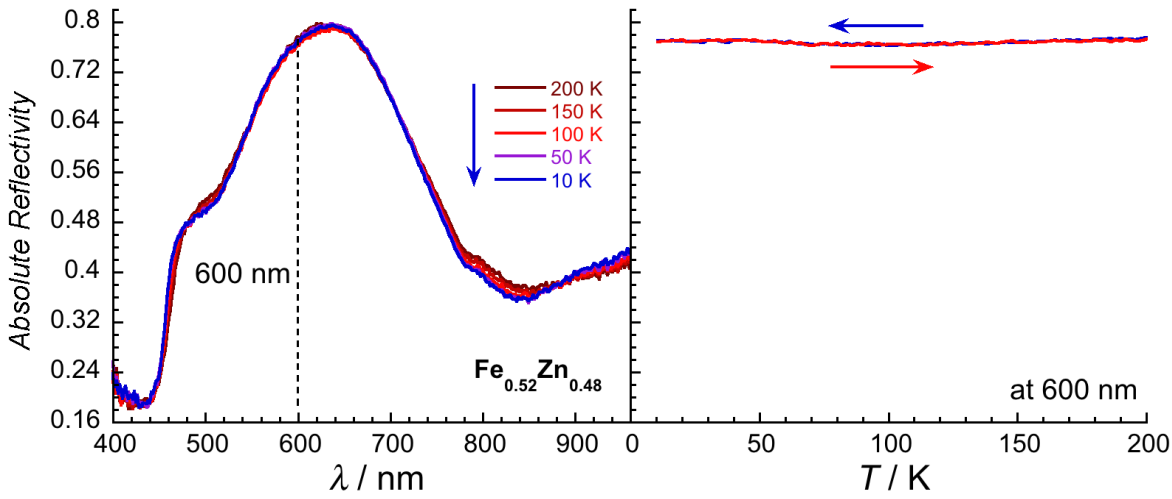

Figure S10. Left: Selected optical reflectivity spectra for **$Fe_{0.52}Zn_{0.48}$** between 200 and 10 K recorded in the dark in cooling mode and at a scan rate of 4 K min^{-1}. Right: Thermal variation of the 600-nm optical reflectivity signal recorded at a scan rate of 4 K min^{-1} when cooling (blue trace) and heating (red trace) in the dark. A spectroscopic white light of 0.08 mW cm^{-2} has been used for these measurements.

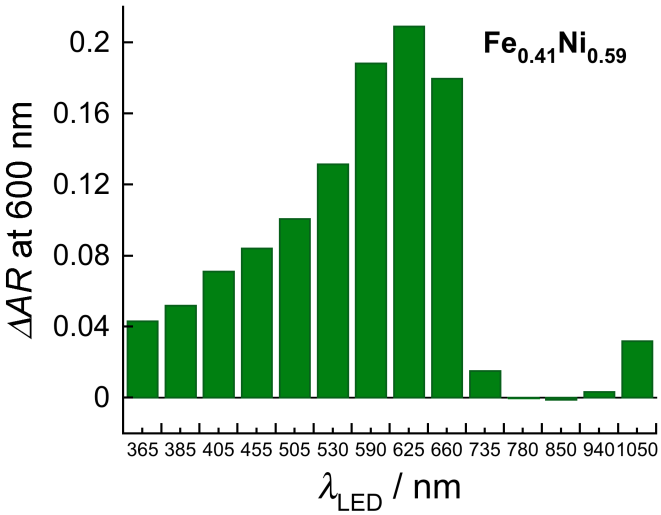

Figure S11. Variation of the absolute optical reflectivity (ΔAR) for **$Fe_{0.41}Ni_{0.59}$** recorded at 600 nm and 10 K (after a fast cooling of the sample from room temperature in the dark) before and after excitation with different LEDs (10 minutes, at 2 mW cm^{-2}). A spectroscopic white light of 0.08 mW cm^{-2} has been used for these measurements.

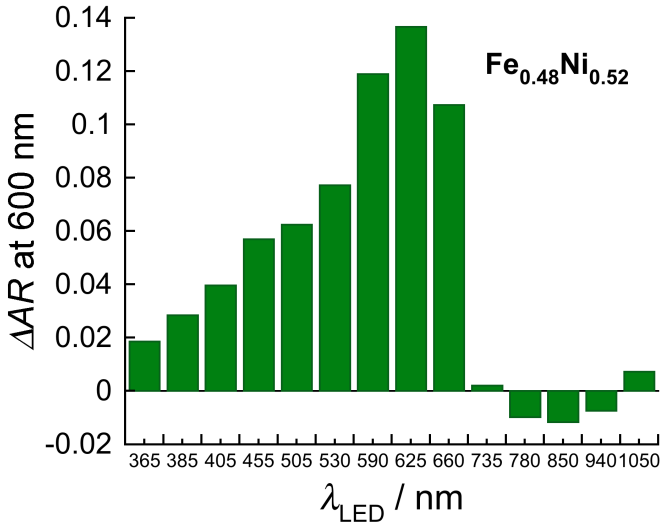

Figure S12. Variation of the absolute optical reflectivity (Δ*AR*) for **$Fe_{0.48}Ni_{0.52}$** recorded at 600 nm and 10 K (after a fast cooling of the sample from room temperature in the dark) before and after excitation with different LEDs (10 minutes, at 2 mW cm^{-2}). A spectroscopic white light of 0.08 mW cm^{-2} has been used for these measurements.

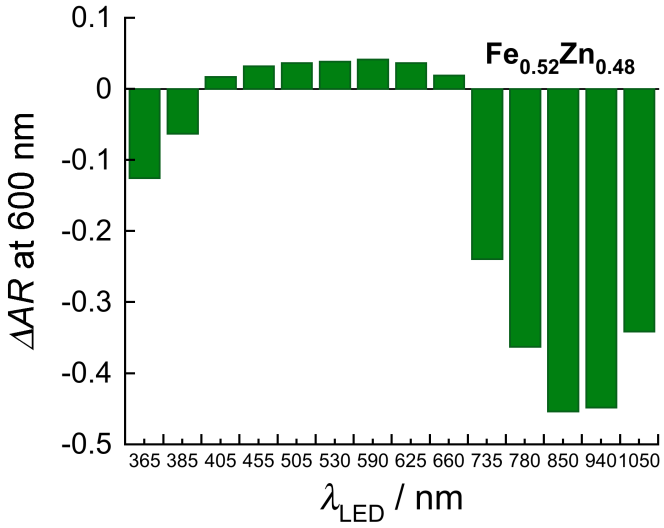

Figure S13. Variation of the absolute optical reflectivity (Δ*AR*) for **$Fe_{0.52}Zn_{0.48}$** recorded at 600 nm and 10 K (after a fast cooling of the sample from room temperature in the dark) before and after excitation with different LEDs (10 minutes, at 2 mW cm^{-2}). A spectroscopic white light of 0.08 mW cm^{-2} has been used for these measurements.

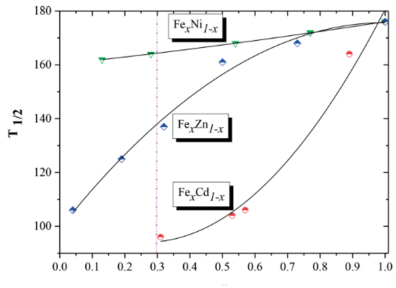

Figure 3. Concentration dependence of the transition temperature $T_{1/2}$ for $[Fe_xNi_{1-x}(Phen)_2(NCS)_2]$, $[Fe_xZn_{1-x}(Phen)_2(NCS)_2]$,[18a] and $[Fe_xCd_{1-x}(Phen)_2(NCS)_2]$.

Eur. J. Inorg. Chem. **2018**, 297–304

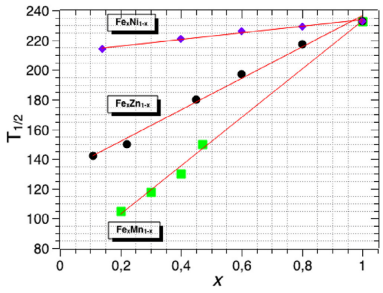

Fig.3. Concentration dependence of the transition temperature $T_{1/2}$ for $[Fe_xNi_{1-x}(bpp)_2](NCSe)_2$, $[Fe_xZn_{1-x}(bpp)2](NCSe)_2$ and $[Fe_xMn_{1-x}(bpp)_2](NCSe)_2$.

Polyhedron **2017**, *123*, 138–144

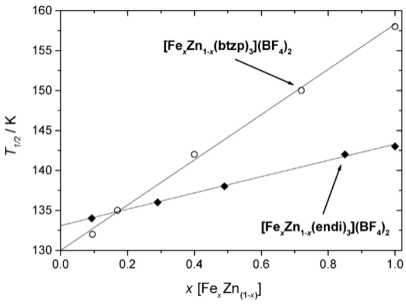

Figure 3. Concentration dependence of the transition temperature $T_{1/2}$ for (o) $[Fe_xZn_{1-x}(btzp)_3](BF_4)_2$ and (◆) $[Fe_xZn_{1-x}(endi)_3](BF_4)_2$. Linear fit appears as a straight line.

Eur. J. Inorg. Chem. **2008**, 34, 5382–5389

Figure S14. Concentration dependence of the $T_{1/2}$ temperature for different families of doped SCO complexes from the litterature.[2-5] Copyright 2018 Wiley; Copyright 2017 Elsevier; Copyright 2008 Wiley.

Table S1. Crystal data and refinement details.

	$[Ni(^{2Me}L)(NCBH_3)_2]$	$[Zn(^{2Me}L)(NCBH_3)_2]$	$Fe_{0.52}Zn_{0.48}$	$Fe_{0.48}Ni_{0.52}$	$Fe_{0.41}Ni_{0.59}$
Temperature / K	123(2)	123(2)	123(2)	123(2)	123(2)
Empirical formula	$C_{18}H_{28}B_2N_6Ni$	$C_{18}H_{28}B_2N_6Zn$	$C_{18}H_{28}B_2Fe_{0.52}N_6Zn_{0.48}$	$C_{18}H_{28}B_2Fe_{0.48}N_6Ni_{0.52}$	$C_{18}H_{28}B_2Fe_{0.41}N_6Ni_{0.59}$
Formula weight / g mol^{-1}	408.79	415.45	410.5	407.41	407.61
Crystal system	Monoclinic	Monoclinic	Monoclinic	Monoclinic	Monoclinic
Space group	*C*2/*c*	C2/c	C2/c	C2/c	C2/c
***a* / Å**	20.137(2)	20.4004(8)	20.388(3)	20.3331(13)	20.368(2)
***b* / Å**	7.7377(4)	7.7841(3)	7.7607(5)	7.7639(4)	7.7635(3)
***c* / Å**	17.2477(17)	15.4651(5)	17.398(3)	17.3470(10)	17.3734(19)
***β* / °**	131.660(17)	123.9830(10)	132.59(3)	132.336(6)	132.480(19)
Volume / Å^3	2007.8(5)	2036.39(13)	2026.7(7)	2024.3(2)	2026.0(6)
Z	4	4	4	4	4
ρ_{calc} / mg mm^{-3}	1.352	1.355	1.345	1.337	1.336
μ / mm^{-1}	1.489	1.221	4.014	3.690	3.319
***F*(000)**	864.0	872.0	864.0	860.0	861.0
Reflections collected	3814	16162	3634	3700	3689
Independent reflections	1956	2237	1961	1950	1961
R_{int}	R_{int} = 0.0207	R_{int} = 0.0233	R_{int} = 0.0371	R_{int} = 0.0271	R_{int} = 0.0265
Goodness-of-fit on F^2	1.069	1.095	1.091	1.139	1.168
Final *R* indexes	R_1 = 0.0331	R_1 = 0.0201	R_1 = 0.0363	R_1 = 0.0365	R_1 = 0.0365
[$I \geq 2\sigma(I)$]	wR_2 =0.0883	wR_2 =0.0518	wR_2 =0.0865	wR_2 =0.0906	wR_2 =0.09325
Final *R* indexes	R_1 = 0.0351	R_1 = 0.0201	R_1 = 0.0417	R_1 = 0.0390	R_1 = 0.0379
[all data]	wR_2 = 0.0907	wR_2 = 0.0521	wR_2 = 0.0896	wR_2 = 0.0917	wR_2 = 0.0933
Largest diff. peak/hole / eÅ^{-3}	0.32/-0.43	0.33/-0.23	0.27/-0.37	0.34/-0.34	0.31/-0.42

Table S2. Selected bond lengths and structural parameters.

	$[Ni(^{2Me}L)(NCBH_3)_2]$	$[Zn(^{2Me}L)(NCBH_3)_2]$	$Fe_{0.52}Zn_{0.48}$	$Fe_{0.48}Ni_{0.52}$	$Fe_{0.41}Ni_{0.59}$
T **/ K**	123	123	123	123	123
Spin state of Fe^{II}	-	-	HS	HS	HS
M-N_{NCBH3} / Å	2.0717(13)	2.1177(12)	2.1339(19)	2.1459(17)	2.1250(18)
M-$N_{pyridine}$ / Å	2.0937(14)	2.1649(11)	2.1718(19)	2.1609(16)	2.1621(17)
M-N_{amine} / Å	2.1550(14)	2.2495(11)	2.2477(18)	2.2332(16)	2.2371(17)
M-$N_{average}$ / Å	2.10	2.17	2.18	2.18	2.17
cis **N-M-N / °**	78.22 (5)-99.25(5)	76.30 (4)-102.76(7)	75.90 (7)-99.71(7)	76.16 (6)-103.15(9)	76.00 (6)-103.43(10)
trans **N-M-N / °**	167.18(5)-176.67(7)	163.10(4)-174.72(6)	162.61(7)-174.36(10)	163.44(6)-174.04(9)	163.18(6)-174.09(10)
Σ **/ °** [a]	63.8(5)	75.8(2)	78.8(4)	77.2(3)	78.32(4)
Θ **/ °** [a]	153.7(5)	189.3(3)	194.0(6)	183.0(6)	186.90(3)
N-C-BH_3 / °	177.18(17)	177.61(15)	178.1(3)	177.8(2)	177.6(2)
M-N-C_{NCBH3} / °	162.69(13)	161.17(11)	161.22(19)	161.95(17)	162.31(17)

[a] *Σ* is the sum of deviations from 90° of the 12 cis N−Fe−N angles; *Θ* is the sum of the deviations from 60° of the 24 possible octahedron twist angles; i.e., *Σ* = 0 and *Θ* = 0 are corresponding to a perfect octahedral site.

Table S3. Comparison of the intermolecular interactions in **Fe**, **[Ni(2^{Me}L)(NCBH$_3$)$_2$]**, **[Zn(2^{Me}L)(NCBH$_3$)$_2$]**, **Fe$_{0.52}$Zn$_{0.48}$**, **Fe$_{0.48}$Ni$_{0.52}$** and **Fe$_{0.41}$Ni$_{0.59}$** at 82 and 123 K. Distances longer than the sum of Van der Waals radii are underlined.

	Fe	**Fe**	**[Ni(2^{Me}L)(NCBH$_3$)$_2$]**	**[Zn(2^{Me}L)(NCBH$_3$)$_2$]**	**Fe$_{0.52}$Zn$_{0.48}$**	**Fe$_{0.48}$Ni$_{0.52}$**	**Fe$_{0.41}$Ni$_{0.59}$**
***T* / K**	82	123	123	123	123	123	123
Spin state of Fe^{II}	LS	HS	-	-	HS	HS	HS
NC<u>B</u>H$_3$···H(pyridine) / Å	2.9234(76)	2.8982(24)	2.927(3)	2.911(3)	2.911(4)	2.909(4)	2.896(4)
N<u>C</u>BH$_3$···H(methylene) / Å	2.6846(43)	<u>2.9023(14)</u>	2.7960(16)	2.8778(16)	2.900(2)	2.875(2)	2.867(2)
NC<u>B</u>H$_3$···H(methyl) / Å	3.031(5)	3.1447(17)	3.120(3)	3.1423(15)	3.149(3)	3.139(3)	3.114(3)
π···π (centroids) / Å	3.7094(4)	3.6254(11)	3.6590(17)	3.6312(12)	3.618(2)	3.631(2)	3.629(2)
C(pyridine)···C(pyridine) / Å	3.3911(60)	<u>3.4229(21)</u>	3.392(2)	<u>3.411(2)</u>	<u>3.406(3)</u>	<u>3.407(3)</u>	<u>3.408(3)</u>
C(methyl)···H(pyridine) / Å	2.8914(54)	<u>2.9509(17)</u>	<u>2.9343(19)</u>	<u>2.948(2)</u>	<u>2.955(3)</u>	<u>2.949(2)</u>	<u>2.940(2)</u>
H(methyl)···H(pyridine) / Å	2.3817(3)	<u>2.4084(1)</u>	<u>2.4146(7)</u>	<u>2.40611(7)</u>	<u>2.4300(12)</u>	<u>2.4126(3)</u>	<u>2.4058(8)</u>
H(methyl)···H(methyl) / Å	2.3933(4)	<u>2.6086(2)</u>	<u>2.5154(6)</u>	<u>2.58315(8)</u>	<u>2.6256(10)</u>	<u>2.5782(2)</u>	<u>2.5871(7)</u>
N<u>C</u>BH$_3$···H(pyridine) / Å	2.8010(36)	2.8281(11)	2.8204(18)	2.8303(13)	2.842(3)	2.838(2)	2.816(2)
NC<u>B</u>H$_3$···H(methyl) / Å	3.1512(48)	3.0447(15)	3.094(3)	3.0550(17)	3.066(3)	3.071(3)	3.055(3)

References:

(1) Ye, Y. S.; Chen, X. Q.; De Cai, Y.; Fei, B.; Dechambenoit, P.; Rouzières, M.; Mathonière, C.; Clérac, R.; Bao, X. Slow Dynamics of the Spin-Crossover Process in an Apparent High-Spin Mononuclear Fe^{II} Complex. *Angew. Chemie Int. Ed.* **2019**, *58* (52), 18888–18891.

(2) Baldé, C.; Desplanches, C.; François Létard, J.; Chastanet, G. Effects of Metal Dilution on the Spin-Crossover Behavior and Light Induced Bistability of Iron(II) in $[Fe_xNi_{1-x}(bpp)_2](NCSe)_2$. *Polyhedron* **2017**, *123*, 138–144. https://doi.org/10.1016/j.poly.2016.08.046.

(3) Sylla, M. S.; Baldé, C.; Daro, N.; Desplanches, C.; Marchivie, M.; Chastanet, G. On the Effect of the Internal Pressure on the Photoinduced Spin-Crossover Behavior of $[Fe_xM_{1-x}$(1,10-Phenanthroline$)_2(NCS)_2]$ Solid Solutions (M = Ni^{II}, Zn^{II},and Cd^{II}). *Eur. J. Inorg. Chem.* **2018**, *2018* (3–4), 297–304. https://doi.org/10.1002/ejic.201700350.

(4) Chakraborty, P.; Enachescu, C.; Walder, C.; Bronisz, R.; Hauser, A. Thermal and Light-Induced Spin Switching Dynamics in the 2D Coordination Network of $\{[Zn_{1-x}Fe_x(bbtr)_3](ClO_4)_2\}_\infty$: The Role of Cooperative Effects. *Inorg. Chem.* **2012**, *51* (18), 9714–9722. https://doi.org/10.1021/ic301006c.

(5) Baldé, C.; Desplanches, C.; Grunert, M.; Wei, Y.; Gütlich, P.; Létard, J. F. Influence of Metal Dilution on the Light-Induced Spin Transition in Two 1D Chain Compounds: $[Fe_xZn_{1-x}(Btzp)_3](BF_4)_2$ and $[Fe_xZn_{1-x}(Endi)_3](BF_4)_2$. *Eur. J. Inorg. Chem.* **2008**, No. 34, 5382–5389. https://doi.org/10.1002/ejic.200800570.